Damköhler number scaling of active cascade effects in turbulent premixed combustion

Jonathan F. MacArt *1 and Michael E. Mueller $^{\dagger 2}$

January 12, 2021

Abstract

Effects of combustion heat release on turbulent velocity and scalar statistics are investigated as a function of the Damköhler number using three Direct Numerical Simulation (DNS) databases of spatially developing turbulent premixed jet flames. At low Karlovitz numbers, where heat-release effects dominate turbulent kinetic energy budgets, their relative significance scales with the integral Damköhler number in a priori Reynolds-Averaged Navier-Stokes (RANS) statistics and the filter Damköhler number in Large Eddy Simulation (LES). The Damköhler-number scaling of counter-gradient transport in this regime follows theoretical arguments underpinning linear-algebraic turbulence models, which explains their efficacy at low Karlovitz numbers. Conversely, at moderate Karlovitz numbers, LES subfilter turbulence is more strongly influenced by heat-release effects than the analogous large-scale RANS turbulence. This is consistent with the notion of an "active cascade," which postulates that heat-release-induced volumetric expansion competes on intermediate scales with classical forward-cascade energy transfer. LES exposes these dynamics as dominant subfilter-scale physics, unlike in RANS, where they are secondary to the effects of mean-shear production at the large scales. The significance of subfilter-scale interactions is promoted by the LES filter itself, which modifies the RANS spectral basis by incorporating local flamenormal averaging. This is highlighted by comparing LES fields obtained using a 3D filter to those using a modified 2D filter, excluding the flame-normal direction, which significantly reduces the apparent influence of heat-release effects but is not representative of LES in practice. The subfilter modeling challenges posed by these distinctions at moderate Karlovitz numbers and order-unity Damköhler numbers remain to be understood.

1 Introduction

Interactions between turbulence and combustion heat release can dramatically alter turbulence dynamics in turbulent premixed combustion. When a flame is thin and fast relative to turbulence scales, combustion-induced pressure-dilatation (volumetric expansion) becomes a significant source of turbulent kinetic energy (TKE) and is balanced by "negative production;" that is, the mean shear "production" term becomes a TKE sink.¹ Negative production has long been associated with counter-gradient transport (CGT),^{2,3} which invalidates the Boussinesq/Smagorinsky and gradient-diffusion assumptions of conventional dissipative turbulence models.^{4,5} This presumably arises in part due to inverse-cascade energy transfer.⁶⁻⁹

Scaling arguments¹⁰ suggest that pressure–dilatation work becomes the dominant source of TKE when the premixed-flame time scale is faster than the viscous dissipation time scale. This dependence may be recast as a local Karlovitz number

$$Ka \equiv \frac{t_F}{t_\eta} = \frac{\delta_F}{s_L} \left(\frac{\epsilon}{\nu}\right)^{1/2} \tag{1}$$

¹Department of Aerospace and Mechanical Engineering, University of Notre Dame, Notre Dame, IN 46556, USA
²Department of Mechanical and Aerospace Engineering, Princeton University, Princeton, NJ 08544, USA

^{*}jmacart@nd.edu

[†]muellerm@princeton.edu

and a critical Karlovitz number $Ka_{cr} \equiv \tau_B$. In these, $t_F \equiv \delta_F/s_L$ is the laminar flame time scale; $t_\eta \equiv (\nu/\epsilon)^{1/2}$ is the Kolmogorov time scale; $\tau_B \equiv \rho_u/\rho_b - 1$ is the flame density ratio; δ_F is the laminar flame thickness; s_L is the laminar flame speed; ν is the kinematic viscosity; ϵ is the TKE dissipation rate; and ρ_u and ρ_b are the densities of the unburned reactants and burned products, respectively.

Effects of combustion-induced dilatation on turbulence, including inverse-cascade energy transfer and CGT, should be apparent for $Ka \ll Ka_{cr}$. Turbulence in this regime essentially undergoes rapid distortion by the flame. $^{3,\,8,\,11-15}$ In the opposite extreme, $Ka \gg Ka_{cr}$, large-scale turbulence straining balances viscous dissipation, and pressure–dilatation work plays a negligible role. $^{5,\,16}$ Although heat release still occurs, it does not significantly disrupt the forward-cascade production–dissipation balance. $^{12,\,17}$

Whereas the forward-cascade picture is disrupted when flame-induced kinetic energy is injected at small scales, *i.e.*, when $Ka \ll Ka_{cr}$, the magnitude of effects felt at large scales depends on the Damköhler number

$$Da \equiv \frac{t_{\ell}}{t_F} = \frac{s_L}{\delta_F} \frac{\ell}{u'},\tag{2}$$

where ℓ is a suitable pseudo-integral length scale and u' is the rms fluctuations. In the early 1990s, Gao and O'Brien¹⁸ recognized its importance when performing some of the first Direct Numerical Simulations (DNS) of turbulent reacting flows. They observed a first-order Damköhler-number dependence of mean scalar correlations for Da ≈ 1 , for this corresponds to comparable reaction and flow time scales. However, they found no Damköhler-number effect on velocity fluctuations due to a constant-density assumption. The influence of the Damköhler number in the low-Karlovitz-number regime is addressed in section 3.

Combining the Karlovitz- and Damköhler-number dependence of heat-release effects, a theory of an intermediate regime has been postulated. It is thought that heat release occurring over scales not small enough to promote an outright inverse cascade (e.g., at moderate Karlovitz numbers, $Ka \gtrsim Ka_{cr}$), but with sufficient strength to affect the large scales (Da = O(1)), can result in competition between a heat-release-induced inverse cascade and the classical, production-driven forward cascade. This has been called an "active cascade."

Still, the dependence of heat-release effects on the Damköhler number remains an open question. It can be recast as a Reynolds-number dependence¹⁹ through

$$Re_t = Da^2 Ka^2, (3)$$

where $\text{Re}_t = u'\ell/\nu$. At Da ≈ 1 and moderate Karlovitz numbers, say Ka ≈ 50 , the required Reynolds numbers are high, out of reach for DNS for the foreseeable future. Analysis of intermediate-regime heat-release effects on large-scale turbulence statistics, for example, in the context of Reynolds-Averaged Navier–Stokes (RANS) closure modeling, will be challenging for the foreseeable future.

Conversely, the influence of heat-release effects in Large Eddy Simulation (LES) at the intermediate scales is characterized by the filter width. This dependence is parameterized by a filter Damköhler number $\text{Da}_{\Delta} \equiv t_{\Delta}/t_F$, where $t_{\Delta} \equiv (\Delta^2/\epsilon)^{1/3}$ is the time scale of turbulence at the filter scale Δ . Unlike the integral-scale Damköhler number, which in general may be varied only by changing the Reynolds number (for fixed Karlovitz number), the filter Damköhler number may be varied by almost two orders of magnitude in a priori analysis by changing the filter width. This enables the Damköhler-number scaling of subfilter-scale heat-release effects to be probed, and insights into active-cascade effects to be obtained, using currently available DNS data.

Building on previous analyses of heat-release effects in the low- and high-Karlovitz-number regimes,⁵ the Damköhler-number dependence of heat-release effects in spatially evolving jet flames is explored in two steps. First, the large-scale Damköhler-number dependence in the Ka \ll Ka_{cr} regime is analyzed using DNS at higher Reynolds number (1.3). Second, the filter-scale Da_{Δ} dependence in the Ka \ll Ka_{cr} and Ka \gtrsim Ka_{cr} regimes is analyzed by varying the Reynolds number and the filter width. Computational configuration details are summarized in section 2. The large-scale Damköhler-number dependence in the low-Karlovitz-number regime is analyzed in section 3. Heat-release effects at varying LES filter scales, with evidence of intermediate-regime and active-cascade effects, are analyzed in section 4. Conclusions are summarized in section 5.

2 Numerical configuration

Spatially evolving, turbulent premixed planar jet flames are simulated using DNS. The low-Mach-number, variable-density Navier–Stokes equations, together with equations for the temperature and the mass fractions of n_s reacting species,

$$\frac{\partial \rho}{\partial t} + \frac{\partial \rho u_j}{\partial x_j} = 0,\tag{4}$$

$$\frac{\partial \rho u_i}{\partial t} + \frac{\partial \rho u_i u_j}{\partial x_j} = -\frac{\partial p}{\partial x_i} + \frac{\partial \tau_{ij}}{\partial x_j},\tag{5}$$

$$\frac{\partial \rho T}{\partial t} + \frac{\partial \rho u_j T}{\partial x_j} = \frac{\partial}{\partial x_j} \left(\frac{\lambda}{c_p} \frac{\partial T}{\partial x_j} \right) + \frac{\lambda}{c_p^2} \frac{\partial c_p}{\partial x_j} \frac{\partial T}{\partial x_j} - \frac{\rho}{c_p} \sum_{k=1}^{n_s} c_{p,k} V_{k,j} \frac{\partial T}{\partial x_j} - \frac{1}{c_p} \sum_{k=1}^{n_s} h_k \dot{m}_k, \tag{6}$$

$$\frac{\partial \rho Y_k}{\partial t} + \frac{\partial \rho u_j Y_k}{\partial x_i} = -\frac{\partial}{\partial x_i} \left(\rho Y_k V_{k,j} \right) + \dot{m}_k, \tag{7}$$

are solved with sufficient resolution such that the small-scale turbulence and flame reaction-zone scales are resolved. In the equations, ρ is the gas density, u_i are the velocity components, p is the hydrodynamic pressure, T is the temperature, and Y_k are species mass fractions. Hydrogen-air combustion is modeled using a 9-species, 50-reaction detailed kinetic model.²⁰ The ideal gas equation of state

$$p_0 = \rho R_0 T \sum_{k=1}^{n_s} \frac{Y_k}{W_k},\tag{8}$$

with p_0 the constant thermodynamic pressure, closes the system. Further details of the governing equations, transport models, and numerical solution may be found in MacArt $et\ al.^5$

The flow evolves in the streamwise (x) and cross-stream (y) directions and is statistically homogeneous in the spanwise (z) direction. The computational domain $\mathbf{x} = \{x, y, z\}$ has extents $x \in [0, L]$, $y \in [-H/2, H/2]$, and $z \in [-W/2, W/2]$. Spatio-temporal (RANS) averages are denoted by angle brackets and are obtained from DNS data by averaging in the z-direction and time. For the density, this is

$$\langle \rho \rangle (x, y) \equiv \frac{1}{W(t_e - t_s)} \int_{t_s}^{t_e} \int_{-W/2}^{W/2} \rho(\mathbf{x}, t) \, dz dt,$$
 (9)

where t_s and t_e are the averaging start- and end-times. Durations $t_e - t_s$ are given for specific configurations in section 2.1. Density-weighted averages $\{\phi\} \equiv \langle \rho \phi \rangle / \langle \rho \rangle$ are computed for all other quantities. Density-weighted fluctuations are represented as $\phi'' \equiv \phi - \{\phi\}$.

Filtered DNS fields are obtained from

$$\overline{\phi}(\mathbf{x},t) \equiv \frac{1}{\Delta^3(\mathbf{x})} \int_{\Omega} G(\mathbf{y}, \mathbf{x}) \phi(\mathbf{x} - \mathbf{y}, t) \, d\mathbf{y}, \tag{10}$$

where $G(\mathbf{y}, \mathbf{x})$ is an inhomogeneous filter with unit support inside a box of size $(\Delta_1, \Delta_2, \Delta_3)(\mathbf{x})$. The local directional filter sizes are integer multiples of the local DNS grid spacing: $\Delta_i(\mathbf{x}) = r_\Delta \Delta_{i,\text{DNS}}(\mathbf{x})$ with $r_\Delta \in \{2, 4, 8, 16, 32, 48, 64\}$. The characteristic local filter size is $\Delta(\mathbf{x}) = (\Pi_i \Delta_i(\mathbf{x}))^{1/3}$. Density-weighted-filtered quantities are denoted by tildes, $\widetilde{\phi} \equiv \overline{\rho \phi}/\overline{\rho}$. A list of averaged, fluctuating, filtered, and derived quantities is given in Table 1.

A reaction progress variable

$$C(\mathbf{x}) \equiv \frac{Y_{\text{O}_2}(\mathbf{x}) - Y_{\text{O}_2,u}}{Y_{\text{O}_2,b} - Y_{\text{O}_2,u}} \tag{11}$$

represents a local, instantaneous flame coordinate, where $Y_{k,u}$ and $Y_{k,b}$ are the mass fractions of species k in unburned reactants and equilibrium products, respectively.

Field	Definition	Description
$\langle \phi \rangle$	(2.6)	Spatio-temporal (RANS) averages
$\{\phi\}$	$\langle \rho \phi \rangle / \langle \rho \rangle$	Density-weighted RANS averages
ϕ''	$\phi - \{\phi\}$	Density-weighted fluctuations
$\overline{\phi}$	(2.7)	Filtered DNS fields
$\frac{\phi''}{\widetilde{\phi}}$	$\overline{ ho\phi}/\overline{ ho}$	Density-weighted filtered DNS fields
R_{ij}	$\{u_i u_j\} - \{u_i\} \{u_j\}$	Reynolds stress $(\S 3.1)$
$F_{j,k}$	$\{u_j Y_k\} - \{u_j\} \{Y_k\}$	Scalar flux (§3.2)
$ au_{ij}^{ ext{ iny SGS}}$	$\widetilde{u_iu_j} - \widetilde{u}_i\widetilde{u}_j$	Subfilter stress $(\S4.1)$
$F_{j,k}^{ ext{SGS}}$	$\widetilde{u_j Y_k} - \widetilde{u}_j \widetilde{Y}_k$	Subfilter scalar flux $(\S4.1)$

Table 1: Notation for RANS and LES averaged and filtered quantities.

	5P-K1	5P-K2	10P-K1
$Re_0 = U_0 H_0 / \nu$	5 000	5 000	10 000
$Da_0 = (s_L/\delta_F)(\ell_0/u_0')$	0.99	0.06	1.40
$\mathrm{Ka}_0 = (\delta_F/s_L)(\nu_0/\epsilon_0)^{1/2}$	10.9	43.5	10.9
$Ka_{\{C\}=0.5}$	3.7	54.0	4.7
H_0 (mm)	4.32	1.08	7.23
$U_0 \text{ (m/s)}$	23.4	93.4	27.8
Domain $(L, H, W)/H_0$	$12 \times 24 \times 3$	$24 \times 16 \times 3$	$12 \times 24 \times 3$
Grid size	$768 \times 586 \times 256$	$1536 \times 576 \times 256$	$1292\times1024\times384$
Duration $(t_e - t_s)U_0/H_0$	62.75	70.56	8.68

Table 2: Jet-flame DNS conditions. Quantities with subscript $(\cdot)_0$ are evaluated in the unburned reactants at the jet outlet. In-flame Karlovitz numbers $Ka_{\{C\}=0.5}$ are reported at streamwise location $x/H_0=3$.

2.1 Jet-flame simulations

An unburned stoichiometric ($\phi = 1.0$) hydrogen-air premixture, diluted 20% by volume with nitrogen to avoid flashback, issues from a central jet at bulk Reynolds number $\text{Re}_0 \equiv U_0 H_0/\nu_0 = 5\,000$ with jet height H_0 and bulk velocity U_0 . The inlet viscosity ν_0 is evaluated in the unburned reactants. Laminar coflow jets of equilibrium products surround the reactants jet. The laminar flame thickness and laminar flame speed at these conditions are $\delta_F = 0.435\,\text{mm}$ and $s_L = 1.195\,\text{m/s}$, respectively. The critical Karlovitz number of the mixture is $\text{Ka}_{cr} = 6.7$.

DNS databases of three configurations are considered. Cases 5P-K1 and 10P-K1 have $Re_0 = 5\,000$ and $Re_0 = 10\,000$, respectively, in-flame Karlovitz number $Ka_{\{C\}=0.5} < Ka_{cr}$, and approximately unity Da_0 . Case 5P-K2 has $Re_0 = 5\,000$, $Ka_{\{C\}=0.5} = O(10Ka_{cr})$, and $Da_0 = 0.06$. "In-flame" properties are evaluated at $\{C\} = 0.5$. Table 2 lists DNS conditions, grid parameters, and fully developed statistics averaging durations. Previously reported studies of 5P-K1 and 5P-K2, as well as further configuration details, may be found in MacArt etal.⁵

2.2 Numerical discretization

The coupled Navier–Stokes, temperature, and reacting species equations are discretized using second-order central differences and staggered variable placement,²¹ except for convective terms in the temperature and species equations, which are discretized using a third-order weighted essentially non-oscillatory (WENO) scheme.²² The equations are integrated in time using a fractional-step method²³ and an iteratively implicit, linearized midpoint method²⁴ with an alternating-direction implicit (ADI) framework for transport terms.

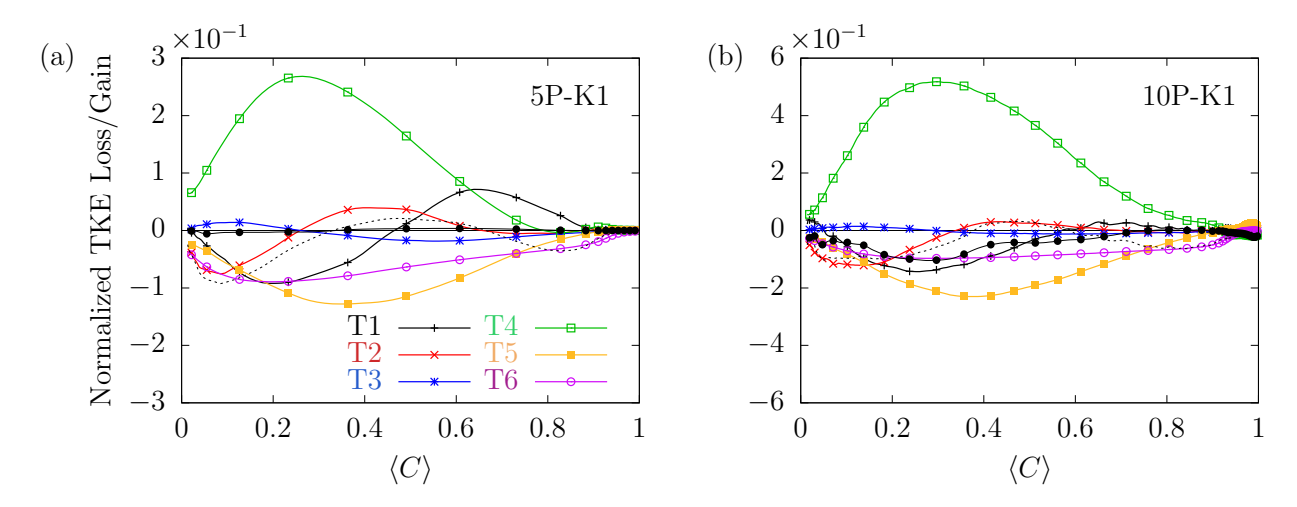


Figure 1: TKE budgets for (a) 5P-K1 and (b) 10P-K1. Major terms are labeled as indicated in the text. The unsteady term is indicated by black lines with points (\bullet), and the residual is indicated by dashed lines. Both cases are are shown at $x/H_0 = 3$.

Reaction source terms in the species and temperature equations are integrated monolithically with transport terms using an approximately factorized exact Jacobian.²⁵

The computational grid resolves the local mean Kolmogorov length scale $\{\eta\} = (\{\nu\}^3/\{\epsilon\})^{1/4}$ to within $\Delta_{i,\text{DNS}}/\{\eta\} = 1.8$ in all cases. The laminar flame thickness is resolved by a minimum of $\delta_F/\Delta_{1,\text{DNS}} = 15$ cells in 5P-K1 and 10P-K1 and a minimum of $\delta_F/\Delta_{3,\text{DNS}} = 20$ cells in 5P-K2. These resolutions are generally considered sufficient for DNS.^{26–29}

3 Damköhler-number scaling of inverse-cascade effects

Damköhler-number effects in the inverse-cascade regime—low Karlovitz number and order-unity integral Damköhler number—are first discussed. For fixed Ka, the integral-scale Damköhler number is adjusted according to (1.3) by changing the Reynolds number. MacArt $et\ al.^5$ reported velocity statistics for 5P-K1; here, these are compared to the new case 10P-K1 with higher Re_t and Da. This corresponds to a relatively faster flame time scale compared to the integral time scale.

3.1 Effect on velocity statistics

The turbulent kinetic energy evolves according to

$$\frac{1}{2} \frac{\partial \langle \rho \rangle \{u_i'' u_i''\}}{\partial t} = -\underbrace{\frac{1}{2} \frac{\partial \langle \rho \rangle \{u_i'' u_i''\} \{u_k\}}{\partial x_k}}_{\text{T1}} - \underbrace{\frac{1}{2} \frac{\partial}{\partial x_k} \langle \rho u_k'' u_i'' u_i'' \rangle}_{\text{T2}} + \underbrace{\frac{\partial}{\partial x_k} \langle u_i'' \tau_{ik} \rangle}_{\text{T3}} - \underbrace{\left\langle u_i'' \frac{\partial p}{\partial x_i} \right\rangle}_{\text{T4}} - \underbrace{\left\langle \rho u_k'' u_i'' \right\rangle \frac{\partial \{u_i\}}{\partial x_k}}_{\text{T5}} - \underbrace{\left\langle \tau_{ik} \frac{\partial u_i''}{\partial x_k} \right\rangle}_{\text{T6}}, \tag{12}$$

with terms representing unsteadiness, mean convective transport (T1), turbulent transport (T2), viscous transport (T3), the velocity fluctuation–pressure gradient correlation (T4), production by the mean shear (T5), and viscous dissipation (T6). Budgets of these terms, normalized by U_0 , H_0 , and ρ_0 , are shown for the low-Karlovitz-number cases in figure 1.

The 5P-K1 and 10P-K1 budgets differ primarily in the relative magnitude of T4 and T5 compared to the remaining budget terms. T4 contains the pressure-dilatation (volumetric expansion) term, ¹⁶ which becomes

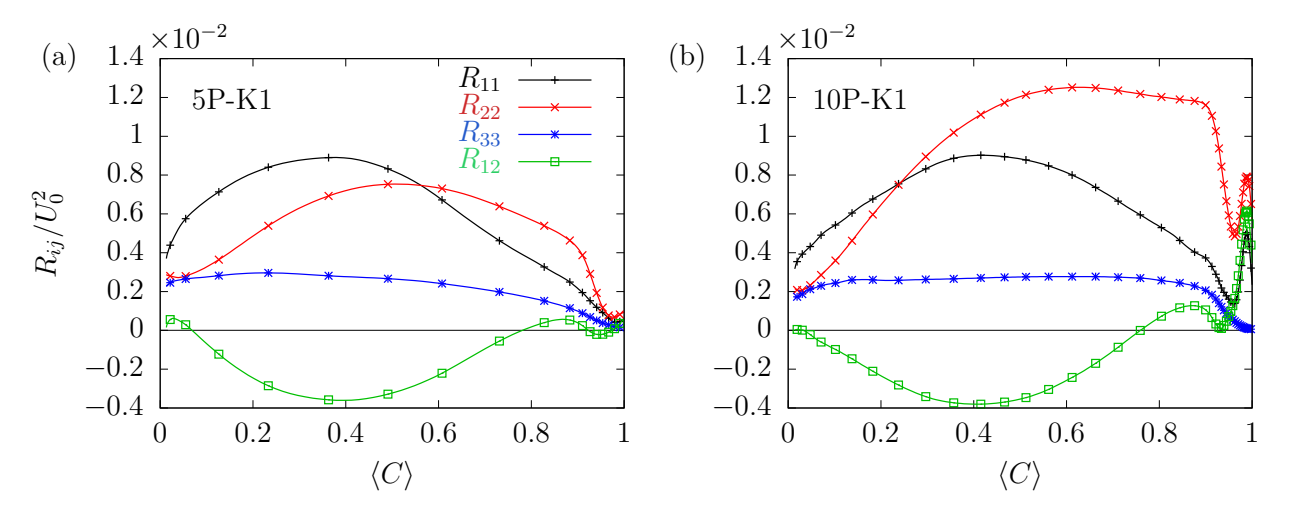


Figure 2: Normalized Reynolds stress components in (a) 5P-K1 and (b) 10P-K1. Both cases are shown at $x/H_0 = 3$.

a significant positive source at $Ka \ll Ka_{cr}$ due to flame-induced expansion. T5, the mean shear "production" term, becomes a TKE sink to balance T4.^{1,5,30} Upon increasing Da (Re_t), T4 and T5 become relatively larger compared to all other terms. This underscores the increasing importance of volumetric-expansion effects with increasing Damköhler number. Said differently, at fixed Karlovitz number, in the regime in which dilatation dominates ($Ka \ll Ka_{cr}$), increasing the Reynolds number likewise increases the Damköhler number, which leads to larger magnitudes of heat-release effects on the turbulence.

This increased significance is further evident from changes to the Reynolds stress $R_{ij} \equiv \{u_i u_j\} - \{u_i\} \{u_j\}$, the nonzero components of which are shown in figure 2. These are qualitatively similar in the two low-Karlovitz-number cases with the exception of the cross-stream R_{22} , which increases more substantially on the burned side at higher Damköhler number (10P-K1). As this component is preferentially aligned with the flame-normal vector (progress-variable gradient),⁵ this larger increase represents a greater magnitude of flame-generated turbulence in agreement with figure 1. Conversely, the magnitude of "counter-Boussinesq" transport⁵ of the shear component R_{12} is essentially unchanged. Apparently, increasing the Damköhler number only increases the thermal expansion effect, while non-equilibrium effects on the Reynolds stress¹⁶ are relatively unaffected.

3.2 The relative significance of "gradient" and "counter-gradient" terms

Implications of heat-release effects for distinctly "gradient" and "counter-gradient" representations of turbulence statistics are now explored. The former corresponds to $Ka \to \infty$ non-reacting turbulence; the latter corresponds to the $Ka \to 0$ infinitely thin flame limit.³ This is done in the context of linear algebraic turbulence models,^{4,5} which comprise linear combinations of terms in the two limit cases. Analysis of these enables exploration of the relative significance of each.

The most basic model for the scalar flux $F_{j,k} \equiv \{u_j Y_k\} - \{u_j\} \{Y_k\}$ in non-reacting turbulent flows is based on the gradient-diffusion hypothesis

$$F_{j,k}^{\text{Grad}} = -\frac{\nu_t}{\text{Sc}_t} \frac{\partial \{Y_k\}}{\partial x_j}, \tag{13}$$

where ν_t is an eddy viscosity. In the following, ν_t is evaluated from a realizable k- ϵ model.^{31,32} The turbulent Schmidt number $Sc_t = 0.65$ is chosen by fitting (3.2) to the 5P-K2 scalar flux, for which it is qualitatively accurate.⁵

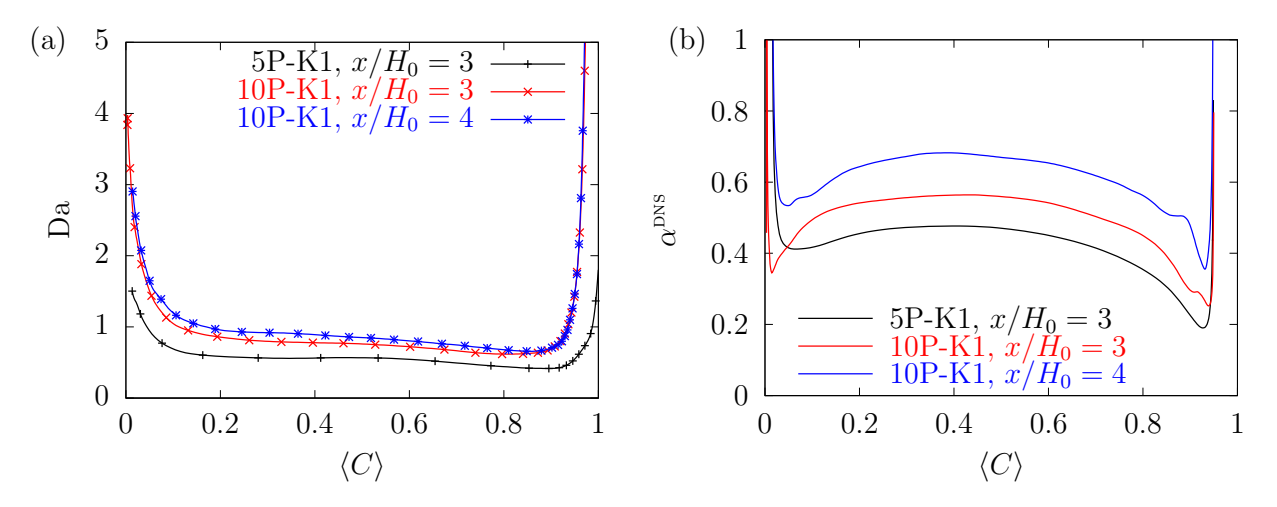


Figure 3: (a) Variation of Da with mean progress variable in 5P-K1 and 10P-K1, shown in the latter at two streamwise coordinates. (b) Variation of the DNS-evaluated efficiency function α^{DNS} within the flame brush at the same coordinates.

The "gradient" term may be combined with a "counter-gradient" term in the thin-flame (Ka \rightarrow 0) limit to form a Linear Algebraic Heat Release (LAHR) model^{4,5}

$$F_{j,k}^{\text{LAHR}} = F_{j,k}^{\text{Grad}} + \alpha \frac{(\{Y_k\} - Y_{k,u})(Y_{k,b} - \{Y_k\})}{Y_{k,b} - Y_{k,u}} \tau s_L \{n_j\},$$
(14)

in which $\{n_j\}$ is the mean flame-normal vector and α is an "efficiency function" that controls the relative weight of the two terms. A functional form of α , which balances the magnitude of the terms in (3.3) at Ka_{cr}, is adopted. It contains a weak Da dependence

$$\alpha = c_{\alpha} \frac{\tau_B}{\tau} \left(\frac{s_L \delta_F}{\nu} \right)^{-1/2} \text{Da}^{1/2}, \tag{15}$$

where $\tau = T_b/T_u - 1$ is a heat-release factor. The model constant is $c_{\alpha} = 1.4$ for consistency with previous work. The model (3.3) with (3.4) qualitatively captures the transition from gradient to counter-gradient transport for the Karlovitz-number range considered here.⁵

Given the DNS data, the left-hand side of (3.3) may be replaced by the exact cross-stream flux $F_{2,k}$ and the "exact" α^{DNS} evaluated. The component $F_{2,k}$ is chosen because it is the only one significantly affected by flame-normal expansion. This is subject to the caveat that α^{DNS} is only truly exact if the gradient-diffusion model (including ν_t evaluation) completely predicts the "gradient" contribution, the thin-flame-limit model completely predicts the "counter-gradient" contribution, and nonlinear interactions are insignificant. Still, the scaling of (3.4) is relatively robust despite the obviously limited framework of (3.3).

At fixed Karlovitz number, the Damköhler number increases by a factor of $\sqrt{2}$ for a factor-of-two increase of Re_t. Figure 3(a) plots Da within the mean flame brush in 5P-K1 and 10P-K1; it is everywhere higher in the latter. The depressed Da within the flame is due to the faster integral time scale (increased TKE), which arises from flame-normal thermal expansion.

Figure 3(b) shows the variation of α^{DNS} with $\{C\}$. The computed values compare favorably with the originally estimated⁴ $\alpha = 0.5$ in the range $0.2 < \{C\} < 0.8$. The flame-normal vector is not preferentially aligned with $F_{i,k}$ outside this range,⁵ thus (3.3) does not adversely affect predictions outside the flame brush.

Figure 4 combines the ordinates of figures 3(a)–(b) to show the Damköhler-number scaling of α^{DNS} . The power of the Da-scaling is indicated by straight lines. Within $0.2 < \{C\} < 0.8$, α^{DNS} scales nearly log-linearly, and its dependence approaches the theoretical Da^{1/2} dependence from (3.4) with increasing

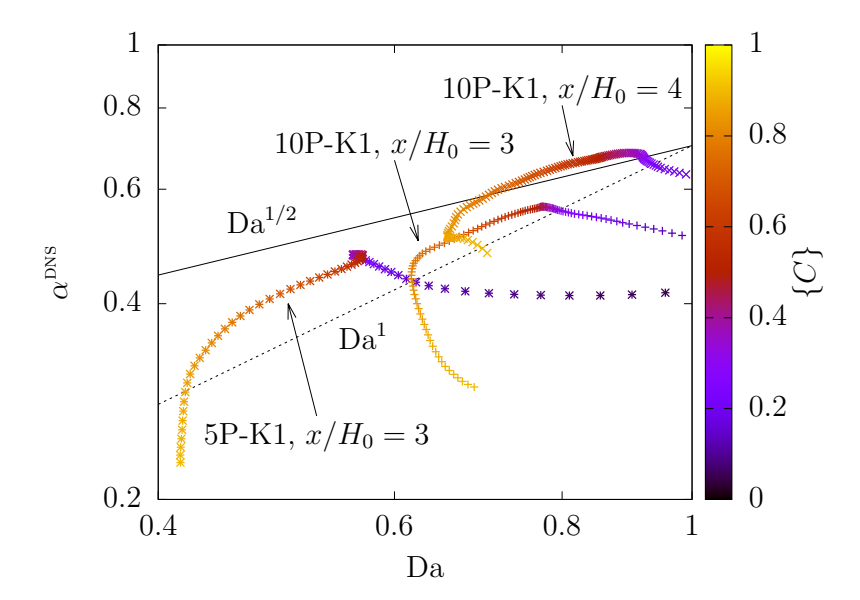


Figure 4: Scaling of the DNS-evaluated efficiency function α^{DNS} with Damköhler number. Statistics in the lower-Reynolds-number case (5P-K1) are shown at $x/H_0=3$. Statistics in the higher-Reynolds-number case (10P-K1) are shown at $x/H_0=3$ and $x/H_0=4$. Points are colored by $\{C\}$. The solid and dashed lines indicate $\text{Da}^{1/2}$ and Da^1 scaling, respectively.

Damköhler number. Therefore, the magnitude of heat-release effects in this low-Karlovitz-number regime is well captured by the assumption of linearly independent gradient and counter-gradient effects. This can be interpreted as a reflection of the significant scale separation between shear production (large scales) and flame-induced volumetric expansion (small scales).

Fundamentally, α has been formulated to link the regime dependence of low-Ka dilatation effects on small-scale turbulence, based on scaling arguments of Bilger, ¹⁰ to experimentally and computationally observed counter-gradient transport. The scaling of α^{DNS} in figure 4 substantiates the claim that algebraic heat-release models can account for counter-gradient transport of statistics for which the *primary* heat-release effects occur via flame-normal thermal expansion. This is true for the flame-normal scalar flux $F_{2,k}$. However, it does not necessarily apply to the Reynolds stress, for which non-equilibrium interactions (e.g., involving pressure-strain redistribution¹⁶) occur over finite flame thickness in low- but nonzero-Karlovitz-number flames. A fundamentally different turbulence-modeling approach is likely necessary to account for these. ^{33, 34}

4 Toward active-cascade effects

While the integral-scale Damköhler number scales the magnitude of heat-release effects on fluctuating quantities, the filter Damköhler number is hypothesized to scale the effect on the analogous subfilter statistics. These are analyzed in section 4.1 for the cases introduced previously, and their scaling with Da_{Δ} is discussed in section 4.2.

4.1 Heat-release effects on subfilter statistics

Subfilter statistics are obtained by filtering DNS data using (2.7). For the cases considered here, t_{Δ} and hence Da_{Δ} generally increase with r_{Δ} and x. The filter time scale $\{t_{\Delta}\}$ is evaluated at $\{\widetilde{C}\}=0.5$ for consistency with Table 2. Subfilter statistics are averaged (2.6) over z and t to capture overall trends. The two statistics of principal interest are the subfilter scalar flux $F_{j,k}^{\mathrm{SGS}} \equiv \widetilde{u_j Y_k} - \widetilde{u}_j \widetilde{Y}_k$ and the subfilter stress $\tau_{ij}^{\mathrm{SGS}} \equiv \widetilde{u_i u_j} - \widetilde{u}_i \widetilde{u}_j$.

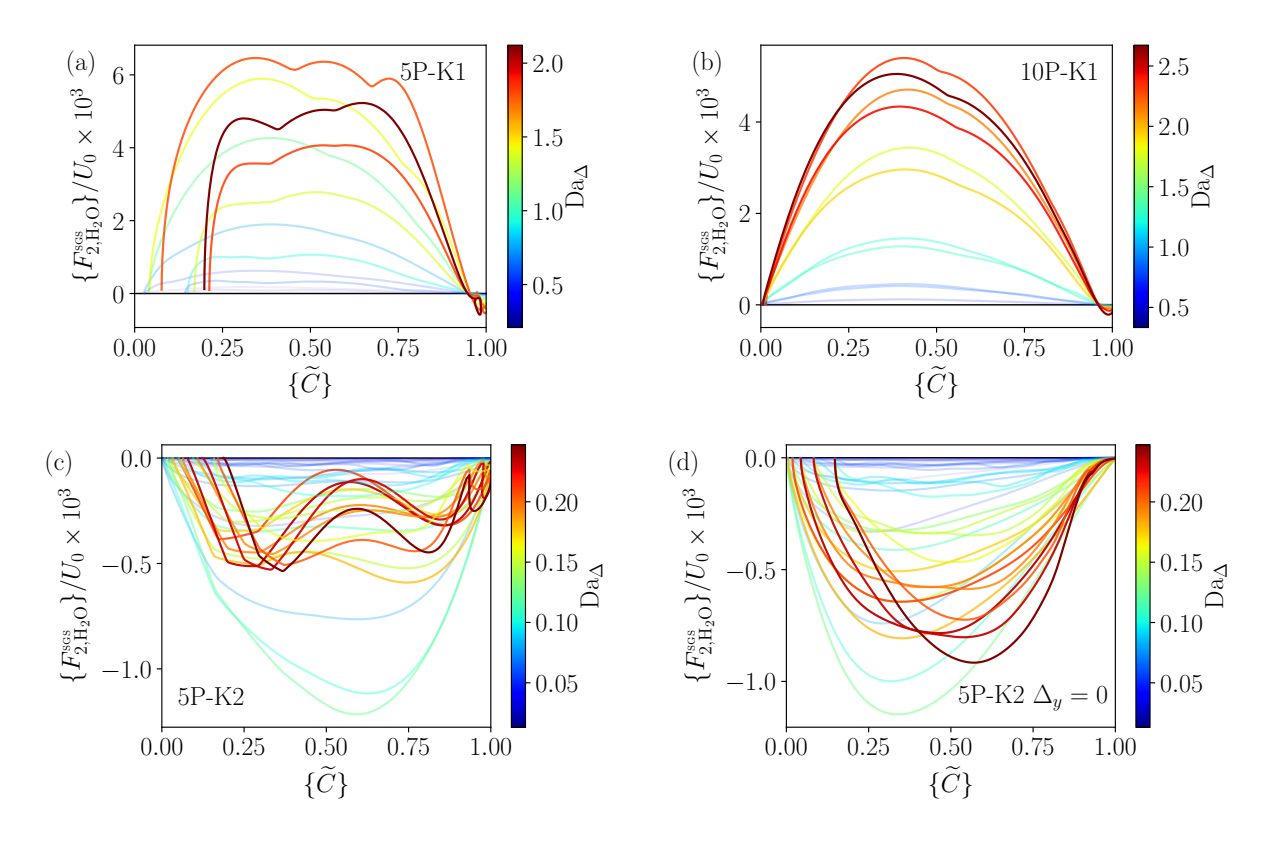


Figure 5: Mean $F_{2,\mathrm{H}_2\mathrm{O}}^{\mathrm{SGS}}$ versus $\{\widetilde{C}\}$ in (a) 5P-K1, (b) 10P-K1, and (c) 5P-K2, for filter ratios $r_{\Delta} \in \{2,4,8,16,32,48,64\}$. Colors denote Da_{Δ} . 5P-K1 and 10P-K1 are shown at $x/H_0 \in \{3,4\}$. 5P-K2 is shown at $x/H_0 \in \{3,6,9,12,15\}$. 5P-K2 with $\Delta_y = 0$ is shown in (d).

4.1.1 Subfilter scalar flux

Figure 5 displays the variation of the mean cross-stream subfilter H_2O mass-fraction flux within the mean flame brush. Since $\partial \{Y_{H_2O}\}/\partial y \geq 0$, positive values of F_{2,H_2O}^{SGS} are considered counter-gradient transport, which is readily apparent for 5P-K1 and 10P-K1. The magnitude of counter-gradient transport in these cases generally increases with Da_{Δ} .

The 5P-K2 subfilter scalar flux (figure 5c) exhibits gradient transport on the whole; this is consistent with past RANS results⁵ and a priori-filtered results for a single Da_{Δ} .³⁵ However, a dependence on Da_{Δ} is apparent. Between $\{C\} = 0.25$ and $\{C\} = 0.75$, the subfilter scalar flux magnitude generally decreases with increasing Da_{Δ} for each filter size r_{Δ} . This would indicate an increase in heat-release effects and countergradient transport as Da_{Δ} increases. While the largest subfilter scalar flux magnitudes do correspond to the largest filter sizes, the basic trend is independent of filter size, depending only on the relative Da_{Δ} increase.

The fact that the 5P-K2 conditions display gradient transport for RANS but trend toward counter-gradient transport for LES is striking. This apparent discrepancy is not inconsistent with the notion of an "active cascade," in that filter-scale energy dynamics may significantly modify LES subfilter turbulence but might not necessarily be strong enough to be felt at the largest turbulence scales in RANS.

The apparent discrepancy can be attributed to an important feature of LES: that filtering fundamentally changes the spectral basis of the energy cascade. The LES filter is effectively a local volume average, even over the inhomogeneous flame-normal direction, while RANS does not average over inhomogeneous directions. Thus, one should not expect LES subfilter quantities to converge to RANS fluctuating quantities

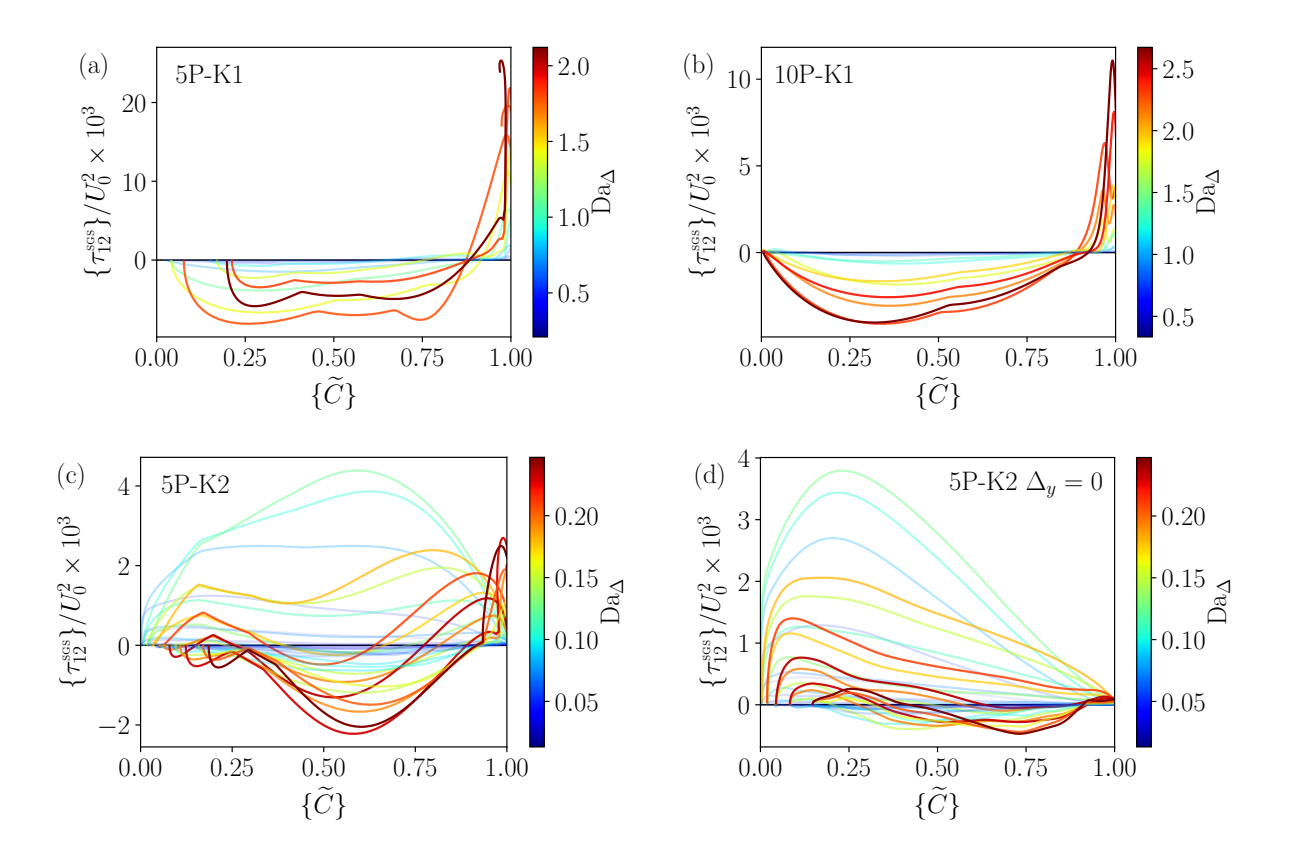


Figure 6: Mean τ_{12}^{sGS} versus $\{\widetilde{C}\}$ in (a) 5P-K1, (b) 10P-K1, and (c) 5P-K2 for filter ratios $r_{\Delta} \in \{2,4,8,16,32,48,64\}$. Colors denote Da $_{\Delta}$. 5P-K1 and 10P-K1 are shown at $x/H_0 \in \{3,4\}$. 5P-K2 is shown at $x/H_0 \in \{3,6,9,12,15\}$. 5P-K2 with $\Delta_y = 0$ is shown in (d).

in the limit of large filter sizes if the filter is performed over inhomogeneous flow directions. Even moderate-Karlovitz-number (nominally thickened) reaction zones can be made mostly or entirely subfilter by large enough Δ . This is evaluated in figure 5(d), for which the cross-stream (flame-normal) component of the filter $\Delta_y = 0$ is disabled. The modified subfilter scalar flux using this 2D filter kernel, which more closely approximates the RANS spectral basis, does not tend toward CGT as for the three-dimensional filter kernel used in figure 5(c).

4.1.2 Subfilter stress

The shear component of the mean subfilter stress, shown in figure 6, follows similar trends. Cases 5P-K1 and 10P-K1 (figures 6a and b) generally exhibit counter-Boussinesq transport of $\{\tau_{12}^{\text{SGS}}\}$ < 0, and the magnitude of the heat-release term increases with Da_{\Delta}.

Conversely, the 5P-K2 subfilter stress (figure 6c) is significantly modified by heat-release effects with increasing Da_{Δ} . It switches from Boussinesq to counter-Boussinesq transport with increasing Da_{Δ} , and the trend is independent of subfilter-stress magnitude. As with the subfilter scalar flux, these effects largely disappear for the 2D filter kernel (figure 6d), but, even still, slight counter-Boussinesq transport remains far downstream for large Da_{Δ} , which is consistent with the downstream R_{12} Reynolds stress at these conditions. Nonetheless, intermediate-regime LES using a 3D filter kernel would be subject to the severe heat-release modifications highlighted by figure 6(c).

4.2 Filter-Damköhler-number scaling of counter-gradient effects

The relative significance of "gradient" and "counter-gradient" subfilter transport is now discussed. In analogy to the Smagorinsky model,³⁶ the simplest model for $F_{j,k}^{SGS}$ is

$$F_{j,k}^{\text{Smag}} = -\frac{(c_s \Delta)^2}{\text{Sc}_t} \widetilde{S} \frac{\partial \widetilde{Y}_k}{\partial x_j}, \tag{16}$$

where $c_s = 0.12$ accurately predicts the 5P-K2 subfilter scalar flux, $\widetilde{S} = (2\widetilde{S}_{ij}\widetilde{S}_{ij})^{1/2}$ is the filtered strain-rate magnitude with $S_{ij} \equiv \frac{1}{2}(\partial u_i/\partial x_j + \partial u_j/\partial x_i)$, and $\operatorname{Sc}_t = 0.65$ as before.

In analogy to the LAHR model in section 3.2, a counter-gradient term obtained in the infinitely-thin flame (Ka \rightarrow 0) limit³ is linearly superimposed with (4.1) to obtain

$$F_{j,k}^{\text{LAHR}} = F_{j,k}^{\text{Smag}} + \alpha_{\Delta} \frac{(\widetilde{Y}_k - Y_{k,u})(Y_{k,b} - \widetilde{Y}_k)}{Y_{k,b} - Y_{k,u}} \tau s_L \widetilde{n}_j, \tag{17}$$

where \tilde{n}_j is a suitable instantaneous filtered-flame-normal vector, and α_{Δ} is the filter-scale efficiency function with a weak Da_{\Delta} dependence:

$$\alpha_{\Delta} = c_{\alpha} \left(\frac{s_L \delta_F}{\nu} \right)^{-1/2} \mathrm{Da}_{\Delta}^{1/2}. \tag{18}$$

Again, this efficiency function is defined to balance the magnitude of terms in (4.2) at Ka_{cr}. The model constant is $c_{\alpha} = 1.4$ as in section 3.2.

The DNS-evaluated $\alpha_{\Delta}^{\text{DNS}}$ is computed in analogy to $\alpha_{\Delta}^{\text{DNS}}$, that is, by substituting the DNS-evaluated $F_{j,k}^{\text{SGS}}$ for the left-hand-side of (4.2) and solving for $\alpha_{\Delta}^{\text{DNS}}$. Instantaneous $\text{Da}_{\Delta}(\mathbf{x},t)$, $\alpha_{\Delta}(\mathbf{x},t)$, and $\widetilde{C}(\mathbf{x},t)$ values for each case and r_{Δ} value are conditionally averaged into filtered-progress variable bins $\widehat{C}(x,y;r_{\Delta},c)$, centered on midpoints $c \in \{0.1,0.2,0.3,0.4,0.5,0.6,0.7,0.8\}$ with bin width 0.1. This range is chosen to avoid the $C \to 0$ non-reacting regions and $\{\widetilde{C}\} > 0.8$ regions of low turbulence intensity (see figure 3a).

The conditionally averaged $\alpha_{\Delta}^{\text{DNS}}$ is shown versus Da_{Δ} in figure 7. It displays a clear $\text{Da}_{\Delta}^{1/2}$ trend for $\text{Da}_{\Delta} = O(10^0)$, which corresponds principally to large values $\alpha_{\Delta}^{\text{DNS}} > 0.2$ and significant counter-gradient transport; see figure 5(a)–(b). The lower-Da_{\Delta} case 5P-K2 does not exhibit $\text{Da}_{\Delta}^{1/2}$ scaling except for the largest filter sizes; these have comparable $\alpha_{\Delta}^{\text{DNS}}$ to the low-Karlovitz-number cases and undergo significant flame modification; see figure 5(c).

Figure 7 underscores the significance of the filter Damköhler number in controlling the prevalence of subfilter heat-release effects on turbulence. Apparently, there is a continuous transition from gradient to counter-gradient subfilter transport with increasing Da_{Δ} , even across the nominally different low- (K1) and moderate-Karlovitz-number (K2) regimes. This can be attributed to the dominant energy-transfer dynamics within the subfilter scales. For small Da_{Δ} , the flame is nearly or fully resolved, even for low-Karlovitz-number flames, hence the subfilter energy transfer resembles the classical forward cascade. Conversely, as Da_{Δ} increases, the flame becomes unresolved, and the influence of heat release must be modeled.

5 Concluding remarks

The principal effect of the integral-scale Damköhler number in the low-Karlovitz-number regime (where heat-release effects dominate) is to intensify the magnitude of flame-induced turbulence production. In TKE budgets, this is manifested principally as increased significance of the pressure-dilatation and negative-production terms relative to other terms, with a concomitant increase in the flame-normal Reynolds stress but no significant changes to the remaining components. Non-equilibrium effects on the Reynolds stress, such as pressure-strain redistribution, do not appear to be intensified as the Damköhler number increases in the low-Karlovitz-number regime.

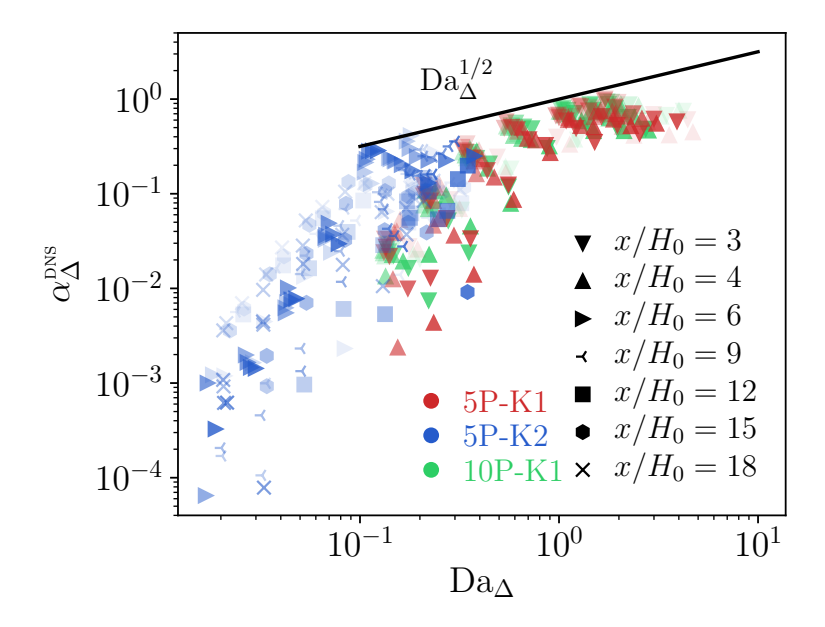


Figure 7: Scaling of $\alpha_{\Delta}^{\text{DNS}}$ with Da_{Δ} . Data from the three cases, denoted by color, are shown at x/H_0 locations indicated by symbols. Point transparency denotes conditionally averaged $\widehat{C} = 0$ (fully transparent) to $\widehat{C} = 1$ (fully opaque). The solid line shows $\text{Da}_{\Delta}^{1/2}$ scaling. Instantaneous quantities are bin-averaged; see section 4.2.

As the primary large-scale effects in the low-Karlovitz-number regime occur due to flame-normal thermal expansion, the prevalence of "gradient" or "counter-gradient" transport of the scalar flux is determined by the integral-scale Damköhler number. This eases the scalar-flux modeling burden in this regime considerably, as has been shown in the context of linear-algebraic closures. Conclusively verifying the effects of increasing scale separation with Reynolds number will require computationally intensive simulations or possibly experimental testing. Finally, further investigation is needed to isolate the non-equilibrium "counter-Boussinesq" Reynolds-stress transport in this regime, which apparently does not scale with the Damköhler number, at least for the range tested.

Likewise, the analogous low-Karlovitz-number filtered statistics exhibit increasing counter-gradient and counter-Boussinesq transport magnitude with increasing filter Damköhler number, and the scaling of the magnitude of counter-gradient effects matches the theoretical $\mathrm{Da}_\Delta^{1/2}$ scaling. This is consistent with the *a priori* suitability of linear-algebraic subfilter closures in this regime.

In the moderate-Karlovitz-number regime, however, heat release more prominently affects the subfilter turbulence in LES than the large-scale fluctuations in RANS. This is due, at least in part, to inherent properties of the LES filter. The LES filter fundamentally changes the spectral basis compared to RANS, with the inclusion of local averaging over inhomogeneous flame-normal scales. This promotes the significance of subfilter energy transfer among wavenumbers principally aligned with these directions. Further research into these inhomogeneous energy-transfer dynamics is needed to better understand the potentially different LES modeling challenge.

Acknowledgments

The authors gratefully acknowledge computational support by the Princeton Institute for Computational Science and Engineering (PICSciE) and the National Energy Research Scientific Computing Center (NERSC) as well as support of the Stanford University Center for Turbulence Research 2018 Summer Program. M.E.M. gratefully acknowledges funding from the National Science Foundation, Award CBET-1839425.

Data Availability

The data that support the findings of this study are available from J. F. MacArt upon request.

References

- [1] R. K. Cheng, Conditional Sampling of Turbulence Intensities and Reynolds Stress in Premixed Turbulent Flames, Combust. Sci. Technol. 41 (1984) 109–142.
- [2] J. B. Moss, Simultaneous Measurements of Concentration and Velocity in an Open Premixed Turbulent Flame, Combust. Sci. Technol. 22 (1980) 119–129.
- [3] K. N. C. Bray, P. A. Libby, G. Masuya, J. B. Moss, Turbulence Production in Premixed Turbulent Flames, Combust. Sci. Technol. 25 (1981) 127–140.
- [4] D. Veynante, A. Trouvé, K. N. C. Bray, T. Mantel, Gradient and counter-gradient scalar transport in turbulent premixed flames, J. Fluid Mech. 332 (1997) 263–293.
- [5] J. F. MacArt, T. Grenga, M. E. Mueller, Effects of combustion heat release on velocity and scalar statistics in turbulent premixed jet flames at low and high Karlovitz numbers, Combust. Flame 191 (2018) 468–485.
- [6] H. Kolla, E. R. Hawkes, A. R. Kerstein, N. Swaminathan, J. H. Chen, On velocity and reactive scalar spectra in turbulent premixed flames, J. Fluid Mech. 754 (2014) 456–487.
- [7] C. A. Z. Towery, A. Y. Poludnenko, J. Urzay, J. O'Brien, M. Ihme, P. E. Hamlington, Spectral kinetic energy transfer in turbulent premixed reacting flows, Phys. Rev. E 93 (2016) 053115.
- [8] J. O'Brien, C. A. Z. Towery, P. E. Hamlington, M. Ihme, A. Y. Poludnenko, J. Urzay, The cross-scale physical-space transfer of kinetic energy in turbulent premixed flames, Proc. Combust. Inst. 36 (2017) 1967–1975.
- [9] J. Kim, M. Bassenne, C. A. Z. Towery, P. E. Hamlington, A. Y. Poludnenko, J. Urzay, Spatially localized multi-scale energy transfer in turbulent premixed combustion, J. Fluid Mech. 858 (2018) 78–116.
- [10] R. W. Bilger, Some Aspects of Scalar Dissipation, Flow, Turbul. Combust. 72 (2004) 93–114.
- [11] A. N. Lipatnikov, J. Chomiak, Effects of premixed flames on turbulence and turbulent scalar transport, Prog. Energy Combust. Sci. 36 (2010) 1–102.
- [12] P. E. Hamlington, A. Y. Poludnenko, E. S. Oran, Interactions between turbulence and flames in premixed reacting flows, Phys. Fluids 23 (2011) 125111.
- [13] P. Brearley, U. Ahmed, N. Chakraborty, A. Lipatnikov, Statistical behaviors of conditioned two-point second-order structure functions in turbulent premixed flames in different combustion regimes, Phys. Fluids 31 (2019) 115109.
- [14] V. A. Sabelnikov, A. N. Lipatnikov, S. Nishiki, T. Hasegawa, Investigation of the influence of combustion-induced thermal expansion on two-point turbulence statistics using conditioned structure functions, J. Fluid Mech. 867 (2019) 45–76.
- [15] C. Kasten, U. Ahmed, M. Klein, N. Chakraborty, Principal strain rate evolution within turbulent premixed flames for different combustion regimes, Phys. Fluids 33 (2021) 015111.
- [16] J. Lee, J. F. MacArt, M. E. Mueller, Heat release effects on the Reynolds stress budgets in turbulent premixed jet flames at low and high Karlovitz numbers, Combust. Flame 216 (2020) 1–8.

- [17] A. J. Aspden, M. S. Day, J. B. Bell, Turbulence-flame interactions in lean premixed hydrogen: transition to the distributed burning regime, J. Fluid Mech. 680 (2011) 287–320.
- [18] F. Gao, E. E. O'Brien, Direct numerical simulations of reacting flows in homogeneous turbulence, AIChE J. 37 (1991) 1459–1470.
- [19] N. Peters, Turbulent Combustion, Cambridge University Press, 2000.
- [20] S. G. Davis, A. V. Joshi, H. Wang, F. Egolfopoulos, An optimized kinetic model of H2/CO combustion, Proc. Combust. Inst. 30 (2005) 1283–1292.
- [21] F. H. Harlow, J. E. Welch, Numerical calculation of time-dependent viscous incompressible flow of fluid with free surface, Phys. Fluids 8 (12) (1965) 2182–2189.
- [22] G.-S. Jiang, C.-W. Shu, Efficient implementation of weighted ENO schemes, J. Comput. Phys. 126 (1996) 202–228.
- [23] J. Kim, P. Moin, Application of a fractional-step method to incompressible Navier-Stokes equations, J. Comput. Phys. 59 (1985) 308–323.
- [24] O. Desjardins, G. Blanquart, G. Balarac, H. Pitsch, High order conservative finite difference scheme for variable density low Mach number turbulent flows, J. Comput. Phys. 227 (2008) 7125–7159.
- [25] J. F. MacArt, M. E. Mueller, Semi-implicit iterative methods for low Mach number turbulent reacting flows: Operator splitting versus approximate factorization, J. Comput. Phys. 326 (2016) 569–595.
- [26] J. B. Freund, S. K. Lele, P. Moin, Compressibility effects in a turbulent annular mixing layer. Part 2. Mixing of a passive scalar, J. Fluid Mech. 421 (2000) 269–292.
- [27] C. Pantano, S. Sarkar, A study of compressibility effects in the high-speed turbulent shear layer using direct simulation, J. Fluid Mech. 451 (2002) 329–371.
- [28] R. Knaus, C. Pantano, On the effect of heat release in turbulence spectra of non-premixed reacting shear layers, J. Fluid Mech. 626 (2009) 67–109.
- [29] E. R. Hawkes, O. Chatakonda, H. Kolla, A. R. Kerstein, J. H. Chen, A petascale direct numerical simulation study of the modelling of flame wrinkling for large-eddy simulations in intense turbulence, Combust. Flame 159 (2012) 2690–2703.
- [30] S. Zhang, C. J. Rutland, Premixed flame effects on turbulence and pressure-related terms, Combust. Flame 102 (1995) 447–461.
- [31] T.-H. Shih, J. Zhu, J. L. Lumley, A Realizable Reynolds Stress Algebraic Equation Model, NASA TM 105993 (1993) 1–34.
- [32] T.-H. Shih, W. W. Liou, A. Shabbir, Z. Yang, J. Zhu, A new k-epsilon eddy viscosity model for high Reynolds number turbulent flows, Comput. Fluids 24 (1995) 227–238.
- [33] J. F. MacArt, T. Grenga, M. E. Mueller, Evolution of flame-conditioned velocity statistics in turbulent premixed jet flames at low and high Karlovitz numbers, Proc. Combust. Inst. 37 (2019) 2503–2510.
- [34] J. Lee, M. E. Mueller, Closure modeling for the conditional Reynolds stresses in turbulent premixed combustion, Proc. Combust. Inst. (in press).
- [35] J. F. MacArt, M. E. Mueller, Scaling and modeling of heat-release effects on subfilter turbulence in premixed combustion, Center for Turbulence Research Proceedings of the Summer Program (2018) 299–308.
- [36] J. Smagorinsky, General circulation experiments with the primitive equations I. The basic experiment, Mon. Weather Rev. 91 (1963) 99–164.